International Journal of Rock Mechanics & Mining Sciences 47 (2010) 962–973

Contents lists available at ScienceDirect

International Journal of Rock Mechanics & Mining Sciences

journal homepage: www.elsevier.com/locate/ijrmms

Evolution of poroelastic properties and permeability in damaged sandstone

D.W. Hu [a,b], H. Zhou [b], F. Zhang [a], J.F. Shao [a,*]

[a] University of Lille, LML, UMR8107, CNRS, Villeneuve d'Ascq, France
[b] IRSM, Chinese Academy of Science, Wuhan, China

ARTICLE INFO

Article history:
Received 18 August 2009
Received in revised form
14 May 2010
Accepted 12 June 2010
Available online 25 June 2010

Keywords:
Poroelasticity
Damage
Permeability
Microcrack
Sandstone
Porous media

ABSTRACT

This paper is devoted to experimental investigation of mechanical behavior, poroelastic properties and permeability in saturated sandstone. The emphasis is to study the evolution of Biot's coefficients and permeability with the growth of microcracks. Basic mechanical responses are first investigated through triaxial compression tests, showing nonlinear stress–strain relations, volumetric dilatancy, pressure sensitivity, elastic modulus degradation and induced anisotropy. Original tests are then performed for the determination of Biot's coefficients in the axial and radial directions at different levels of stress. It is shown that the evolution of Biot's coefficient is clearly anisotropic in nature due to the oriented closure of initial microcracks and growth of induced microcracks. The rock permeability in axial direction is also measured for different values of stress; it decreases in the first stage with the closure of microcracks and then progressively increases due to the opening of induced microcracks. However, the permeability significantly increases only when the coalescence of microcracks occurs.

© 2010 Elsevier Ltd. All rights reserved.

1. Introduction

It is essential to account for the coupling between pore pressure variation and rock deformation for the stability and durability analysis in many engineering applications, such as integrity of underground and surface structures, geological storage of nuclear wastes, sequestration of carbon and residual gas, oil and gas production in complex conditions. One of the tasks consists in the determination of Biot's coefficient in different loading condition, which is the main parameter of poroelasticity theory [1,2]. Further, the evolution of pore pressure is inherently related to fluid flow in pore space. It is then also primordial to evaluate the variation of rock permeability as a function of applied stress and subsequent rock deformation. Various experimental investigations have been so far reported on the determination of Biot's coefficient and permeability in different rocks [3–10]. Some other works have been performed on the effective stress concept for poroelastic modeling in rock materials [11,12]. However, most of these works have focused on the study of poroelastic and flow properties of rocks at initial (undamaged) state or under hydrostatic stress state. However, most brittle rocks (sandstone, limestone, granite, etc.) exhibit deviatoric stress induced damage due to the nucleation and propagation of microcracks [13–17]. The main consequences of the induced damage include nonlinear stress–strain relations, degradation of elastic properties and induced anisotropy, volumetric dilatancy, material softening and permeability variations [18–24]. A number of laboratory investigations have contributed to the evaluation of permeability during rock damage and cracking, for instance [25–33]. Recently, some interesting works have also been performed on the coupling between pore collapse, grain crushing and permeability as well as wave velocity evolution in highly porous sandstones [34,35]. In a similar way, the anisotropy and dispersion of elastic waves in cracked rocks have also been investigated [36]. These works have clearly shown that the rock permeability (and wave velocity) evolution is directly related to the distribution, opening and coalescence of induced microcracks. However, there are very few experimental investigations on the determination of poroelastic properties with the evolution of rock damage. This is the main purpose of the present work. We propose to investigate the evolution of Biot's coefficient in a typical brittle rock (sandstone) at different levels of the deviatoric stress during triaxial compression tests. For the completeness, the variation of rock permeability is also studied. The present paper is organized as follows. After a short description of physical properties of the studied rock, the basic mechanical behaviour of the sandstone is first studied. Original laboratory tests are then presented for the determination of Biot's coefficients in the axial and radial directions at different levels of deviatoric stress. The variation of rock permeability is studied in the last part of the paper.

2. Description of sandstone

The rock studied in the present work is a red sandstone from the Zhejiang province in China. The average porosity is about 21%; the density under dry and saturated conditions is 2.17 and

* Corresponding author.
E-mail address: Jianfu.shao@univ-lille1.fr (J.F. Shao).

1365-1609/$ - see front matter © 2010 Elsevier Ltd. All rights reserved.
doi:10.1016/j.ijrmms.2010.06.007

Table 1
Mineral compositions of red sandstone.

Composition	Content (%)	Grain radius (mm)
Quartz	55	0.02–0.35
Feldspar	33	0.02–0.15
Mica	5	0.002–0.02
Calcite	4	0.002–0.02
Chlorite	2	0.02–0.07
Montmorillonite	1	0.02–0.07

2.35 g/cm^3, respectively. The petrophysical analysis with the X-ray diffraction technique shows that the main mineral compositions of the sandstone are quartz, feldspar, mica and calcite, as shown in Table 1. The microscopic analysis of microstructure is also performed with the SEM technique. The quartz and feldspar grains are ovoid and surrounded by mica and calcite. This morphology results in a continuous pore network, which constitutes the connected porosity for interstitial fluid flow. The sandstone can be considered as a porous medium in the sense of Biot's theory.

3. Experimental device and procedure

Different laboratory tests will be performed in this work, including hydrostatic compression, monotonous triaxial compression, triaxial compression with unloading–reloading cycles for the determination of Biot's coefficient and permeability measurements. Thermal effects are not studied here and all the tests will be carried out under isothermal conditions with the room temperature of 20 ± 2 °C.

The samples are cored from a big block without macroscopic cracks. The block was carefully cut from an intact layer in situ formation. Cylindrical samples used were 50 ± 0.1 mm in diameter and 100 ± 0.5 mm in height. According to the average size of mineral grains, this sample size seems to be reasonable to represent a representative volume element of the sandstone. There is the presence of moderate parallel bedding planes in the sandstone, leading to a slightly transverse isotropic structure. The emphasis here is to study poroelastic properties with induced anisotropic microcracks. The slight initial anisotropy of the sandstone is not taken into account. All the samples are thus drilled in the direction perpendicular to the bedding planes.

The saturation condition is an important factor for the determination of poroelastic properties. Thus, the sample is first saturated with distilled water in vacuum condition before each test. The sample is then inserted inside a rubber jacket and thus isolated from confining fluid. It is placed between two porous steel pads, in order to obtain a uniform distribution of fluid pressure at the inlet and outlet faces of the sample. In addition, after the application of confining pressure, the saturation of the sample is again verified by the injection of water from the inlet face until the set up of a uniform counter pressure inside the sample.

All the tests are conducted with the home-designed autonomous thermal-hydromechanical and chemical (THMC) coupling testing system in conventional triaxial conditions. The schematic illustration of the testing cell is shown in Fig. 1. The axial strain is measured by two LVDT transducers, which are placed between the bottom and top platens inside the cell (Fig. 1). The radial (or lateral) strain is measured by a home-designed strain ring placed at the middle height of the sample. The detailed description of the radial strain ring is given in [37]. Two porous plastic (Teflon) sheets are placed between the sample faces and steel pads in order to reduce the friction effects.

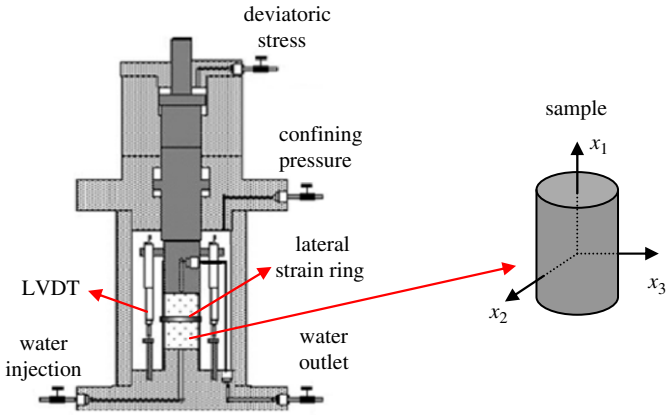

Fig. 1. Autonomous and self-compensated triaxial testing cell and the coordinate frame of sample.

Throughout the paper, the rock mechanics sign convention will be used. The positive sign will be given to compressive stresses and strains. Further, a fixed frame of coordinates will be used for the cylinder sample as shown in Fig. 1. σ_i and ε_i ($i=1,2,3$) denote the three principal stresses and strain while p is the interstitial pressure.

4. Hydrostatic compression test and initial Biot's coefficient

Hydrostatic compression tests are first performed in order to determine the compressibility of sandstone and the initial value of Biot's coefficient in its initial state. Two loading paths are considered.

In the first path, the hydrostatic stress is increased with the constant rate of 8×10^{-3} MPa/s in drained condition with $\Delta p=0$. This load rate is chosen according to rock permeability in order to avoid pore overpressure generated by hydrostatic stress. Typical stress–strain curves are presented in Fig. 2. The axial strain is slightly bigger than the radial (or lateral) one. This confirms the small structural anisotropy of the sandstone. Further, both the axial and radial strains exhibit a nonlinear phase during the first stage of loading. Such a nonlinearity may be attributed to the progressive closure of initial microcracks and bedding planes. One recovers a linear response phase after a certain value of hydrostatic stress, say about 18 MPa. This linear phase should represent the elastic behaviour of sandstone in hydrostatic condition. The volumetric strain is simply calculated by $\varepsilon_v=\varepsilon_1+2\varepsilon_3$ and shown on the same figure. From the linear phase of volumetric strain curve, it is easy to calculate the bulk modulus in drained condition noted by K_b with the relation:

$$K_b=\left(\frac{\Delta\sigma_m}{\Delta\varepsilon_v}\right)_{\Delta p=0} \quad (1)$$

On the other hand, in the second loading path, hydrostatic stress and pore pressure are simultaneously increased with the same increment ($\Delta p=\Delta\sigma_m$). The objective here is to determine the compressibility modulus of the solid skeleton (or solid matrix) of sandstone noted by K_s. Typical stress–strain curves are shown in Fig. 2. We also observe some slight anisotropy on the axial and radial strains and a small nonlinear phase at the beginning of loading. This seems to show that the slight structural anisotropy of sandstone is mainly related to oriented microstructure of the solid matrix. And there exists some isolated microcracks inside the solid matrix contributing to the nonlinear response of this one. After the calculation of the volumetric strain, the compressibility modulus of the solid matrix can be calculated from the

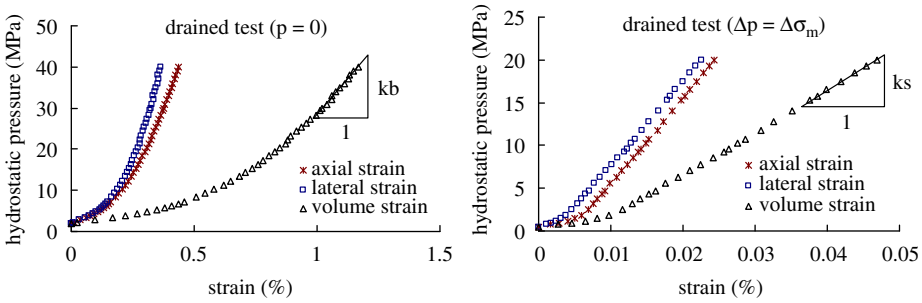

Fig. 2. Stress–strain curves in hydrostatic compression tests with two different loading conditions.

Table 2
Initial values of compressibility moduli and Biot's coefficient of sandstone.

K_b (MPa)	K_s (MPa)	b
6905	50,548	0.86

linear phase by

$$K_s = \left(\frac{\Delta\sigma_m}{\Delta\varepsilon_v}\right)_{\Delta\sigma_m = \Delta p} \tag{2}$$

As mentioned above, the slight structural anisotropy is neglected here and the initial state of sandstone is assumed to be isotropic one. According to the relations between Biot's coefficient and compressibility properties of constituents [2,33,34], the initial Biot's coefficient of sandstone noted by b is given by

$$b = 1 - \frac{K_b}{K_s} \tag{3}$$

For the sandstone studied, the initial values of drained bulk modulus, compressibility modulus of solid matrix and Biot's coefficient are summarized in Table 2.

5. Drained triaxial compression tests

In order to investigate basic mechanical behaviour of sandstone, monotonous triaxial compression tests are now performed in drained conditions and under different values of confining pressure. All the tests are conducted in axial strain controlled conditions. The average strain rate is 3×10^{-6}/s, chosen as low as enough to avoid excessive interstitial over pressure and to verify the condition ($\Delta p=0$). Five values of confining pressure are used such as 0, 5, 10, 20 and 30 MPa. In Fig. 3, the axial, radial and volumetric strains are shown as functions of the deviatoric stress ($\sigma_1-\sigma_3$). The obtained results are quite representative for a brittle rock such as sandstone.

The mechanical response of the sandstone is strongly dependent upon confining pressure. Under low confining pressure, in particular in uniaxial compression test ($\sigma_2=\sigma_3=0$), there exists some nonlinear phase at the beginning of deviatoric loading. This nonlinear phase is attributed to the progressive closure of initial microcracks in the axial direction. With the increase of confining pressure, such a nonlinear phase disappears due to the fact that the initial microcracks are almost closed during the application of confining pressure. Also, under low confining pressure, the sample failure is marked by a sharp peak stress, due to the coalescence of microcracks leading to the splitting of sample. Under higher confining pressures, the peak stress is much less pronounced and even disappears. The failure of sample is generally associated with the onset of shear or compaction bands [19,15,23]. There is a clear transition from brittle to ductile behaviour with confining pressure increase. The failure mechanisms of brittle rocks have also been illustrated through acoustic emissions in [38].

For all confining pressures, after a more and less marked linear stress–strain phase, we observe nonlinear responses of material before and after the peak stress. The nonlinear inelastic strains are directly related to the nucleation and growth of microcracks and mainly generated by the frictional sliding along cracks surfaces.

There is a clear transition from volumetric compressibility to dilatancy for almost all the confining pressures considered here. However, the transition occurs much earlier and the volumetric dilatancy is more important under low confining pressures than higher ones. The transition points at which $\dot{\varepsilon}_v=0$ on the volumetric strain curves are plotted in Fig. 4. It is clear that the transition threshold is dependent on the confining pressure, as that illustrated in some previous works [16]. Physically, the volumetric dilatancy in brittle rocks under compressive stresses may be related to the normal opening of microcracks generated by frictional sliding along rough crack surfaces. And such an opening is influenced by the normal stress to the crack surface, which depends on the confining pressure.

In Fig. 4, we have also reported the values of peak failure stress as functions of confining pressure. For the reason of completeness, the values of failure stress obtained from the tests presented in the later sections are also presented. We can see that the failure line is nonlinear for the regime of low confining pressures and progressively becomes quasi linear for higher ones. This indicates that the failure condition of sandstone is more sensitive to confining pressure when its value is low. For the purpose to get some indicative values of failure parameters, we tried to represent the failure stresses of sandstone by the classical linear Mohr–Coulomb criterion. The following values are obtained for the material cohesion and frictional angle: $C=6.3$ MPa and $\tan\phi=0.684$. These values seem to be consistent with those found in the previous works on sandstones [16,17,25,35,38].

6. Determination of Biot's coefficient in damaged material

In this section, specific triaxial compression tests are performed in order to investigate the evolution of Biot's coefficient with induced damage. The theoretical background used for the interpretation of test data is first defined.

6.1. Theoretical background

The theoretical background for the interpretation of Biot's coefficient is based on the poroelastic theory for anisotropic materials, for instance [39–42]. The poroelasticity has also been extended to brittle rocks with induced anisotropic damage in [43,44]. Based on these previous works, the following theoretical

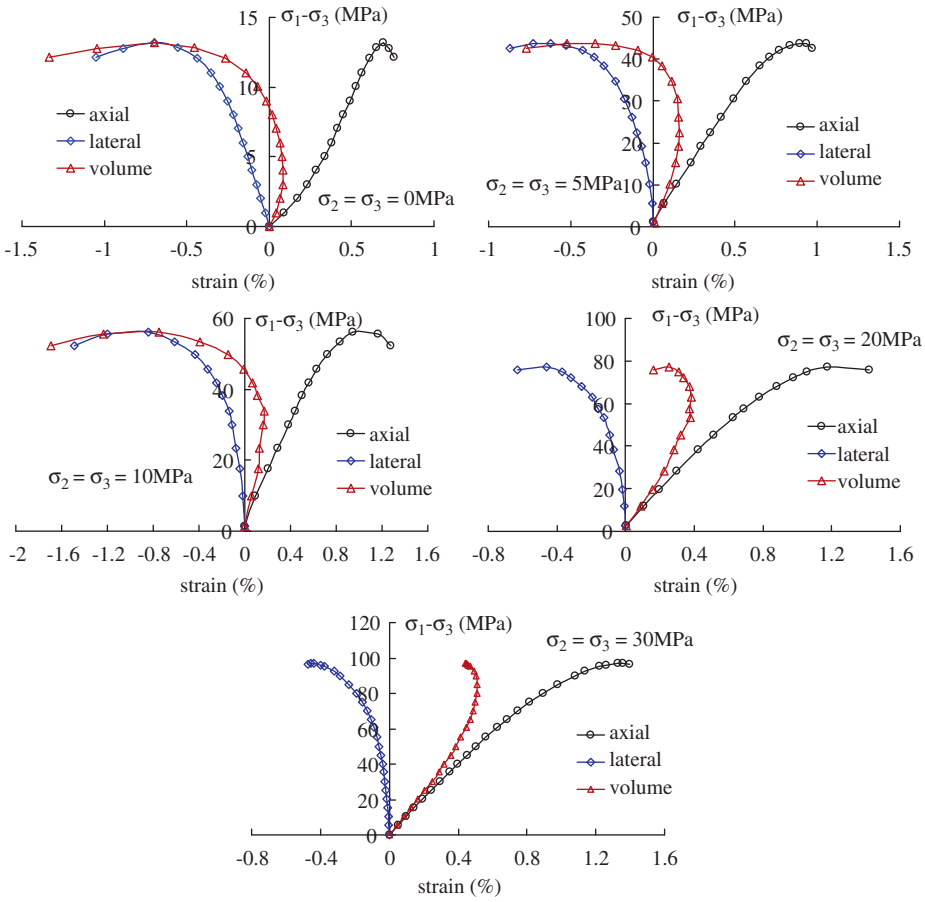

Fig. 3. Stress–strain curves of sandstone in drained triaxial compression tests under different confining pressures.

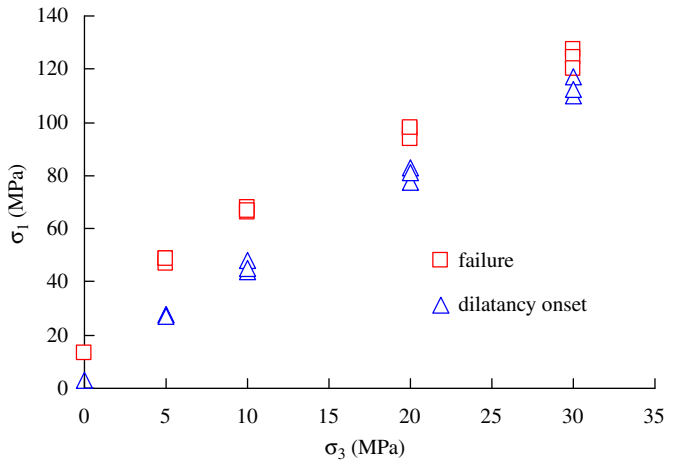

Fig. 4. Experimental values of peak stresses and dilatancy onset stresses, with the data obtained from the three series of tests (monotonous, "cyc1" for determination of Biot's coefficients and "cyc2" for permeability determination).

relations will be used for the determination of Biot's coefficient in damaged sandstone.

Consider a cylinder sample of sandstone with a given distribution of microcracks or a given state of damage. For the sake of simplicity, the macroscopic consequences of arbitrarily distributed microcracks are represented in an equivalent way by those of three orthogonal families of parallel microcracks. Therefore, the damage state may be represented by a second order tensor denoted by (**d**). In general, the damaged material exhibits an orthotropic behaviour and the material symmetry axes correspond to the three principal directions of the damage tensor. In the case of conventional triaxial compression tests, due to the axi-symmetric conditions, the principal directions of damage are defined by the global coordinate frame (Fig. 1). The major damage (d_1) direction coincides with the axial direction of cylinder sample (x_1) and we have $d_2=d_3$. The damaged material exhibits a transverse isotropic behaviour and the isotropy plane is defined by $0x_2x_3$. The general formulation of poroelastic relations for damaged materials is as follows:

$$\sigma_{ij} = C^b_{ijkl}(\mathbf{d})\varepsilon_{kl} - b_{ij}(\mathbf{d})p \tag{4}$$

C^b_{ijkl} and b_{ij} are components of the drained elastic stiffness tensor and Biot's coefficient tensor, respectively, depending on the current damage state (**d**). For the sake of simplicity and without loosing generality, the initial interstitial pressure is set to be zero. Inverting the relations (4) and then applied to the case of conventional triaxial test, the following reduced formulation is obtained:

$$\begin{pmatrix}\varepsilon_1\\ \varepsilon_2\\ \varepsilon_3\end{pmatrix} = \begin{bmatrix}\frac{1}{E^b_1} & \frac{-\nu^b_{12}}{E^b_2} & \frac{-\nu^b_{13}}{E^b_3}\\ \frac{-\nu^b_{21}}{E^b_1} & \frac{1}{E^b_2} & \frac{-\nu^b_{23}}{E^b_3}\\ \frac{-\nu^b_{31}}{E^b_1} & \frac{-\nu^b_{32}}{E^b_2} & \frac{1}{E^b_3}\end{bmatrix}\begin{pmatrix}\sigma_1 - b_1 p\\ \sigma_2 - b_2 p\\ \sigma_3 - b_3 p\end{pmatrix} \tag{5}$$

E^b_i and ν^b_{ij} denote drained Young's modulus and Poisson's ratio of anisotropic damaged material. Consider now some specific loading paths without additional evolution of damage ($\Delta d_i=0$) and keeping the stresses to constant values ($\Delta\sigma_i=0$). The

incremental strains can be expressed as functions of incremental interstitial pressure as follows:

$$\begin{pmatrix}\Delta\varepsilon_1\\ \Delta\varepsilon_2\\ \Delta\varepsilon_3\end{pmatrix}=\begin{pmatrix}1/H_1\\ 1/H_2\\ 1/H_3\end{pmatrix}\Delta p \tag{6}$$

The coupling coefficients H_i are given by

$$\begin{cases}\dfrac{1}{H_1}=\dfrac{b_1}{E_1^b}-\dfrac{v_{12}^b b_2}{E_2^b}-\dfrac{v_{13}^b b_3}{E_3^b}\\ \dfrac{1}{H_2}=-\dfrac{v_{21}^b b_1}{E_1^b}+\dfrac{b_2}{E_2^b}-\dfrac{v_{23}^b b_3}{E_3^b}\\ \dfrac{1}{H_3}=-\dfrac{v_{31}^b b_1}{E_1^b}-\dfrac{v_{32}^b b_2}{E_2^b}+\dfrac{b_3}{E_3^b}\end{cases} \tag{7}$$

It is clear that the values of H_i depend on the damage state of material. Taking into account the symmetry conditions, we have $b_2=b_3$, $E_2^b=E_3^b$, $v_{12}^b=v_{13}^b$, $v_{21}^b=v_{31}^b$ and $v_{23}^b=v_{32}^b$. The two independent coupling coefficients are given by

$$\begin{cases}\dfrac{1}{H_1}=\dfrac{b_1}{E_1^b}-\dfrac{2v_{13}^b b_3}{E_3^b}\\ \dfrac{1}{H_2}=\dfrac{1}{H_3}=-\dfrac{v_{31}^b b_1}{E_1^b}+\dfrac{(1-v_{32}^b)b_3}{E_3^b}\end{cases} \tag{8}$$

The inversion of these relations allows the calculation of Biot's coefficients from the measurable quantities during laboratory tests, that is

$$\begin{cases}b_1=\dfrac{E_1^b}{1-v_{32}^b-2v_{31}^b v_{13}^b}\left(\dfrac{1-v_{32}^b}{H_1}+\dfrac{2v_{13}^b}{H_3}\right)\\ b_3=\dfrac{E_3^b}{1-v_{32}^b-2v_{31}^b v_{13}^b}\left(\dfrac{1}{H_3}+\dfrac{v_{31}^b}{H_1}\right)\end{cases} \tag{9}$$

Therefore, the determination of Biot's coefficients consists in the measurement of effective elastic properties as well as two coupling coefficients for different damage states (or for different levels of deviatoric stress). The testing procedure of such determination is presented in the next section.

6.2. Testing procedure

According to the relations (9), for the determination of Biot's coefficients, the laboratory tests consist in the measurement of two elastic moduli E_1^b and E_3^b, three Poisson's ratios v_{31}^b, v_{13}^b and v_{32}^b, and the two coupling parameters H_1 and H_3, for different levels of deviatoric stress. Note that the Biot's coefficients given in (9) are determined for a given damage state. This means that the measurement of the elastic parameters and coupling coefficients should be performed during an elastic loading process without additional damage evolution. This is done by proceeding in unloading–reloading cycles during triaxial tests. The testing procedure is described as follows and schematically illustrated in Fig. 5.

1. The confining pressure is set up to the desired value under drained condition.
2. The axial strain is increased with a fixed rate and the corresponding deviatoric stress is monitored, while the confining pressure is kept constant.
3. When the deviatoric (or axial) stress reaches a desired value corresponding to certain state of damage, an unloading–reloading cycle of axial stress is proceeded. The unloading–reloading phase corresponds to poroelastic response of material without damage evolution; the poroelastic relations (5) and (6) can be used. During the unloading of axial stress, the radial stress (or confining pressure) and interstitial pressure remain unchanged. The incremental strains are given by $\Delta\varepsilon_1=\Delta\sigma_1/E_1^b$ and $\Delta\varepsilon_3=(-v_{31}^b\Delta\sigma_1)/E_1^b$. This leads to the determination of E_1^b and v_{31}^b.
4. After the unloading of axial stress to certain chosen value (see Fig. 5), the axial stress is hold at this value and we increase the radial stress to some incremental value (the final radial stress remains lower than the axial stress) and measure the variations of axial and radial strains, which are related to the variation of radial stress by $\Delta\varepsilon_1=(-2v_{13}^b\Delta\sigma_3)/E_3^b$ and $\Delta\varepsilon_3=(1-v_{32}^b)\Delta\sigma_3/E_3^b$. At the end of this step, the radial stress is back to its initial value. This step leads to the determination of the quantities v_{13}^b/E_3^b and $(1-v_{32}^b)/E_3^b$.
5. An incremental variation of interstitial pressure is now applied by water injection into the sample while keeping the axial and radial stresses constant. Note that the magnitude of pressure variation should be small in order to avoid additional growth of microcracks and to keep the loading step in elastic range. The variations of axial and radial strains are measured as functions of pressure variation and the following relations hold: $\Delta\varepsilon_1=\Delta p/H_1$ and $\Delta\varepsilon_3=\Delta p/H_3$. At the end of this step, the injected water is outlet and the interstitial pressure is back to its initial value. During this step, the values of the two coupling coefficients (H_1,H_3) can be easily determined.

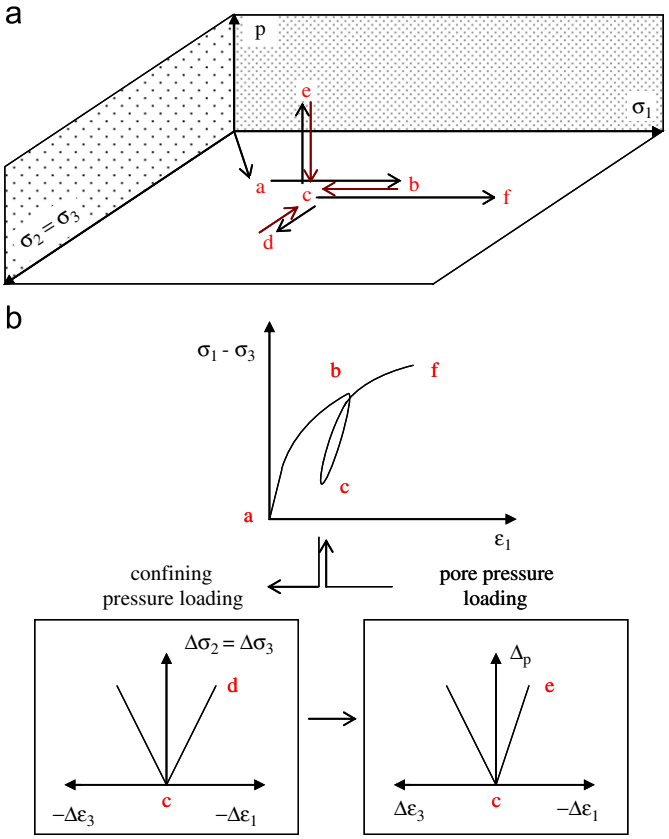

Fig. 5. Schematic illustration of loading path for the determination of Biot's coefficients at different levels of deviatoric stress: (a) stress and pressure path and (b) corresponding strain measurement.

By the combination of these loading steps, we should determine seven parameters with only six measured quantities. More precisely, in the step of radial compression, we should determine three elastic parameters with only two measured strains. In order to overcome this difficulty, we propose the

following simplification. The Poisson's ratio corresponding to the isotropic plane, say v_{23}^b, is not significantly affected by the induced damage and remains at the initial value of undamaged material. This initial value is easily determined from the linear part of stress–strain curves in a triaxial compression test and the average value is found to be $v_{23}^b = 0.23$. Such a simplification seems to be plausible in triaxial compression conditions due to the fact that the induced microcracks are mainly oriented in the axial direction. This simplification is also supported by some previous works [34,36].

6.3. Test results and analysis

A series of four tests are performed with the confining pressures of 5, 10, 20 and 30 MPa. Typical results are plotted in Figs. 6–9. As the emphasis is to study poroelastic properties, pay our attention to the curves of strain variation due to interstitial pressure change. We can see that the variations of strain are clearly anisotropic between the axial and radial directions, in particular under high values of deviatoric stress (high levels of damage). The variation of axial strain is more important than the radial one. This means that the Biot's coefficient in the axial direction (b_1) becomes higher than the radial one (b_3). The anisotropy of Biot's coefficients is in correlation with the fact that the induced microcracks are mainly oriented in the axial direction.

For more details, the experimental values of elastic parameters and coupling coefficients are reported in Tables 3–6, respectively. for the four values of confining pressure. The evaluated values of Biot's coefficients are also given in these tables. For more clarity, the evolutions of elastic moduli and Biot's coefficients with the relative axial strain are given in Figs. 10 and 11.

Under low values of the axial strain, i.e. when the induced damage is still negligible, the difference of elastic modulus between the axial direction (E_1^b) and radial direction (E_3^b) is quite small. And this difference is smaller as the confining pressure is higher. This confirms the slight structural anisotropy of the sandstone and this one is progressively attenuated by the confining pressure due to the closure of bedding planes and initial microcracks. However, at the same time, the values of elastic moduli increase with the confining pressure due to such compaction effects.

In Fig. 10, we can see that the axial modulus increases in the first stage and then decrease when the axial peak strain is reached. This means that the elastic modulus in the axial direction is not clearly deteriorated by the induced damage. This may be explained by the fact that most induced microcracks are mainly parallel to the axial direction. On the other hand, the radial elastic modulus is decreasing almost continuously with the relative axial strain and the growth of induced damage. The deterioration of the radial modulus is much more significant than the axial one, indicating an important induced anisotropy on the elastic properties of sandstone. Moreover, the deterioration of the radial elastic modulus is more important under low confining pressures. This indicates that the effects of induced damage on the macroscopic mechanical behaviour of sandstone are smaller under high confining pressures. This is in conformation with the transition from brittle to ductile behaviour in brittle rocks. However, according to some previous studies on the acoustic emission and wave velocity evolution in cracked rocks [35,36,38], this does not imply that the density of induced microcracks is smaller under high confining pressures. Indeed, the macroscopic properties of porous sandstones such as the effective elastic modulus can be affected by complex coupling effects between the growth of microcracks and pore collapse for instance.

We look now at the evolution of Biot's coefficients in the axial and radial directions. Under low axial strains, i.e. in undamaged or moderate damage state, the Biot's coefficient in the axial direct (b_1) is higher than that in the radial direction (b_3). This confirms the existence of bedding planes (which are perpendicular to the cylinder axis) in the initial state of sandstone. In a logic way, the difference of Biot's coefficient between the two directions is largely attenuated with the confining pressure; this is well correlated with the closure of bedding planes. Another interesting phenomenon is that the values of Biot's coefficients at small axial strains (considered as undamaged or moderate damage state) decrease quite significantly with confining pressure; this is also correlated with the closure of initial bedding planes and microcracks.

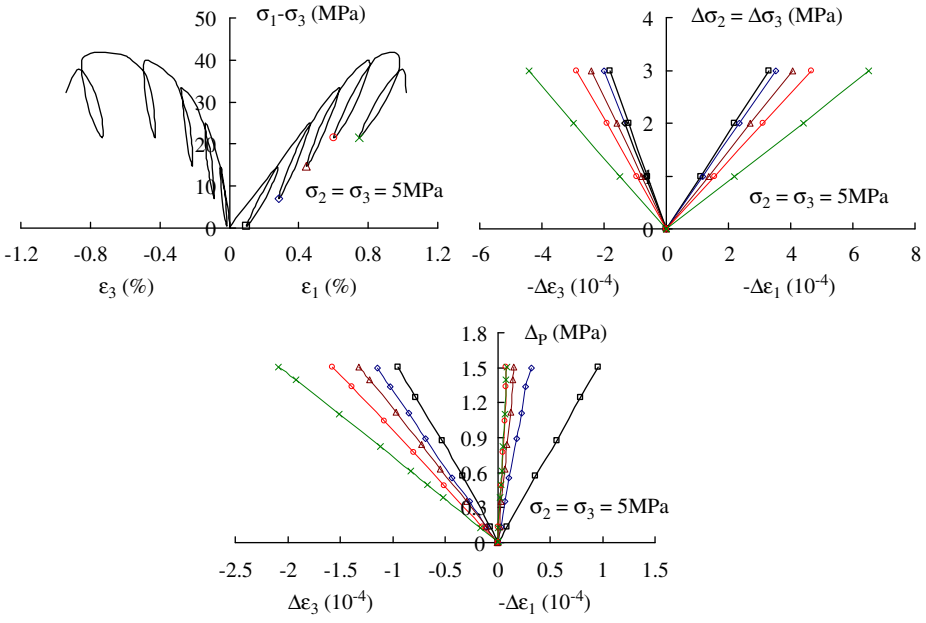

Fig. 6. Stress–strain curves in triaxial compression test under 5 MPa confining pressure and variations of strains due to radial stress and interstitial pressure variations for the identification of elastic properties and coupling coefficients.

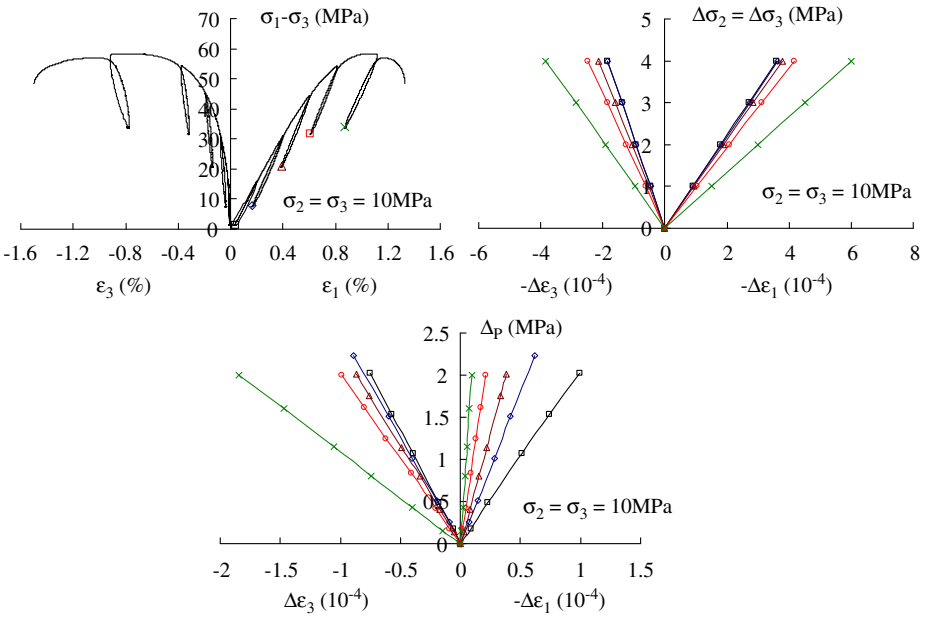

Fig. 7. Stress–strain curves in triaxial compression test under 10 MPa confining pressure and variations of strains due to radial stress and interstitial pressure variations for the identification of elastic properties and coupling coefficients.

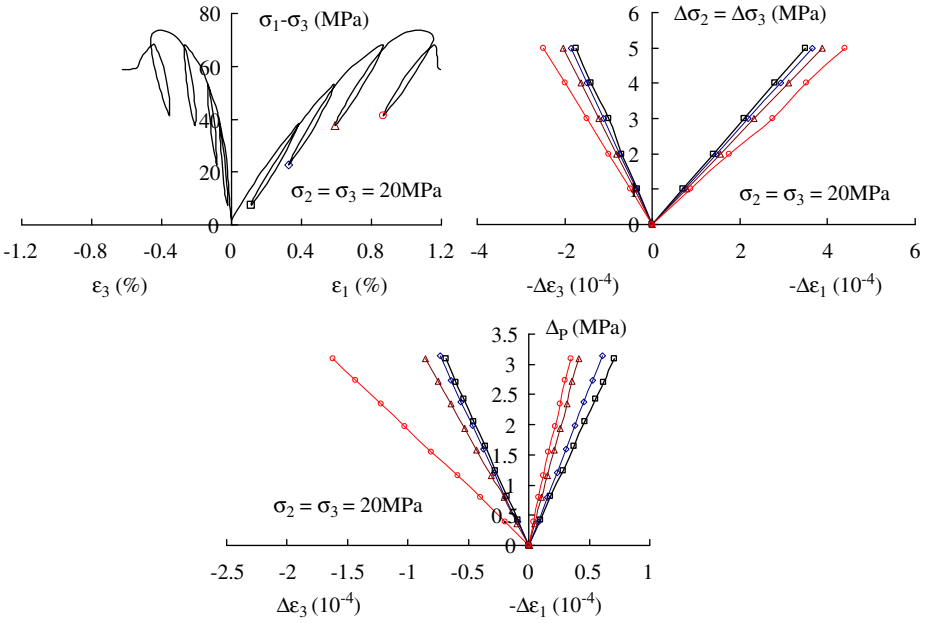

Fig. 8. Stress–strain curves in triaxial compression test under 20 MPa confining pressure and variations of strains due to radial stress and interstitial pressure variations for the identification of elastic properties and coupling coefficients.

Under higher axial strains, the Biot's coefficients are affected by the induced damage. In an average way, the Biot's coefficient in the axial direction (b_1) is at most of the times decreasing with the axial strain. This decrease is associated with the progressive closure of bedding planes and initial microcracks, which are perpendicular to the axis (x_1). Induced microcracks are developed essentially in the direction parallel to the axis (x_1). Therefore, the Biot's coefficient (b_1) is not affected by the induced damage. Only under a very high level of load and damage, approaching to the coalescence of microcracks, the Biot's coefficient (b_1) is affected by the induced damage and increases with the axial strain, for instance in the test with 5 MPa confining pressure. On the other hand, the Biot's coefficient in the radial direction (b_3) is almost continuously increasing and significantly affected by the induced damage. However, the rate of increase is lower when the confining pressure is higher.

Under low confining pressures, say 5 and 10 MPa, and at the high values of deviatoric stress, the evaluated value of Poisson's ratio ν_{31}^{b} is higher than 0.5 and that of Biot's coefficients higher than 1.0 (see the last rows of Tables 3 and 4). A particular attention should be paid to such evaluated values. From a theoretical point of view, in anisotropic materials, the values of Poisson's ratios may be greater than 0.5 and the bound for the Biot's coefficients is $\mathrm{tr}(\mathbf{b})/3 \leq 1$. However, in brittle rocks such as sandstones, the coalescence of microcracks and onset of strain localization bands generally takes place around the peak stress.

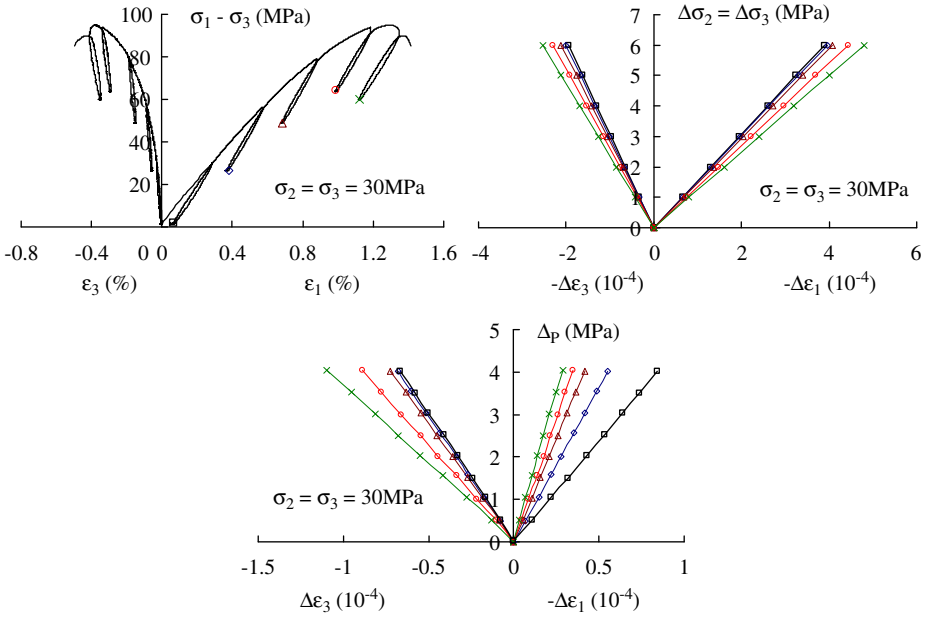

Fig. 9. Stress–strain curves in triaxial compression test under 30 MPa confining pressure and variations of strains due to radial stress and interstitial pressure variations for the identification of elastic properties and coupling coefficients.

Table 3
Evolutions of elastic properties and Biot's coefficients with axial strain in triaxial compression test with the confining pressure of 5 MPa.

ε_1 (%)	E_1^b (MPa)	E_3^b (MPa)	ν_{31}^b	ν_{13}^b	H_1 (MPa)	H_3 (MPa)	b_1	b_3
0.28	7967	6991	0.2	0.21	15,776	15,770	0.877	0.777
0.46	10,257	6525	0.27	0.22	47,793	13,099	0.784	0.823
0.66	9358	5727	0.372	0.23	96,971	11,401	0.756	0.877
0.84	8363	4845	0.501	0.242	12,2720	9594	0.901	0.997
0.98	6802	3563	0.631	0.256	167,630	7182	1.157	1.143

Table 4
Evolutions of elastic properties and Biot's coefficients with axial strain in triaxial compression test with the confining pressure of 10 MPa.

ε_1 (%)	E_1^b (MPa)	E_3^b (MPa)	ν_{31}^b	ν_{13}^b	H_1 (MPa)	H_3 (MPa)	b_1	b_3
0.20	9158	8544	0.16	0.197	20,485	26,912	0.677	0.544
0.40	10,384	8450	0.189	0.195	36,386	24,991	0.549	0.549
0.61	9907	8094	0.191	0.216	42,427	20,064	0.572	0.641
0.81	9145	7374	0.234	0.231	56,171	16,275	0.582	0.732
1.12	8013	5095	0.538	0.243	144,370	10,881	0.789	0.960

Table 5
Evolutions of elastic properties and Biot's coefficients with axial strain in triaxial compression test with the confining pressure of 20 MPa.

ε_1 (%)	E_1^b (MPa)	E_3^b (MPa)	ν_{31}^b	ν_{13}^b	H_1 (MP)	H_3 (MPa)	b_1	b_3
0.382	11,352	11,002	0.177	0.191	43921	44,988	0.421	0.412
0.598	11,250	10,508	0.183	0.196	49165	42,698	0.400	0.409
0.879	10,313	9899	0.226	0.202	52185	35,963	0.395	0.470
1.153	9305	8624	0.285	0.215	74680	22,619	0.422	0.641

The fields of displacement and strain become discontinuous inside the sample. Therefore the strains measured by the axial LVDT and radial ring are no more representative of the average deformation of the sample. The values of poroelastic coefficients evaluated using the strains measured in the localized regime cannot be interpreted as material responses of sandstone.

Table 6
Evolutions of elastic properties and Biot's coefficients with axial strain in triaxial compression test with the confining pressure of 30 MPa.

ε_1 (%)	E_1^b (MPa)	E_3^b (MPa)	ν_{31}^b	ν_{13}^b	H_1 (MP)	H_3 (MPa)	b_1	b_3
0.29	11,945	11,831	0.106	0.191	47,380	59,883	0.371	0.308
0.59	13,457	11,652	0.139	0.196	72,488	58,690	0.326	0.309
0.90	12,776	11,291	0.154	0.202	96,899	55,473	0.273	0.313
1.21	12,024	10,392	0.204	0.215	116,860	45,150	0.270	0.361
1.35	11,188	9586	0.235	0.191	138,710	36,662	0.276	0.412

However, for the reason of completeness of experimental data, all the obtained values are shown in tables.

It is also interesting to note that the observation on Biot's coefficient evolution is strikingly in agreement with the observations of Sayers and Kachanov [45] in sandstones and of Schubnel and Guéguen [36] in granite on the evolution of anisotropic crack densities prior to macroscopic failure. This suggests that it will be possible to develop some analytical formulations of the Biot coefficients in terms of a crack density tensor in future works on constitutive modeling of poromechanical behaviour in cracked rocks.

7. Variation of permeability

As mentioned in Introduction, a number of previous works have shown that the permeability of brittles rocks can significantly change due to the evolution of microstructure [25–32,46]. Therefore, for the completeness of the present work, the variation of permeability during triaxial compression tests is here investigated in addition to the poroelastic properties.

7.1. Testing procedure

Two different experimental techniques are usually used for the measurement of rock permeability: the steady-state flow (or permanent regime) method and pulse test (or transient regime) technique. The choice of the one or the other method mainly

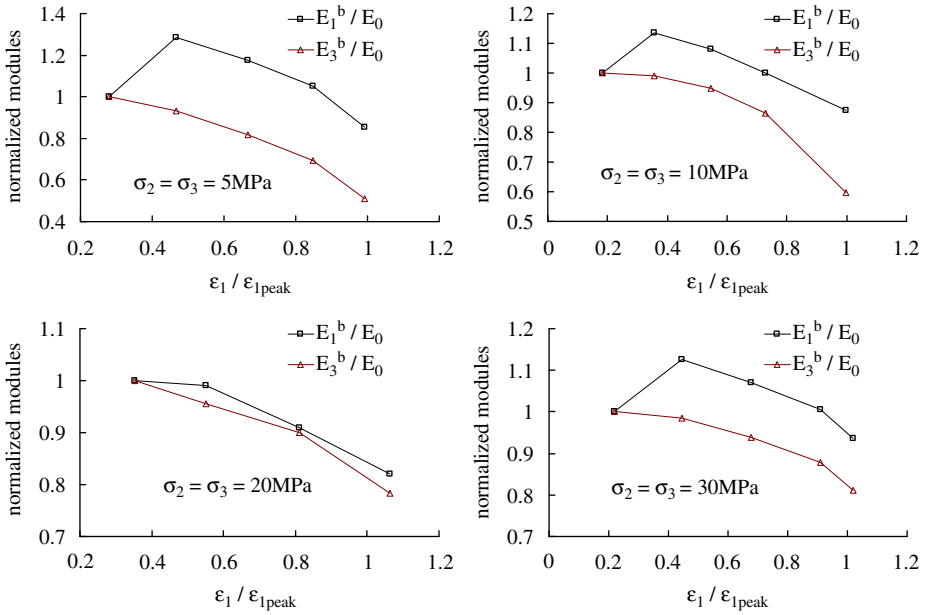

Fig. 10. Evolutions of elastic modulus in axial and radial directions with relative axial strain in triaxial compression tests with different confining pressures for the determination of Biot's coefficients.

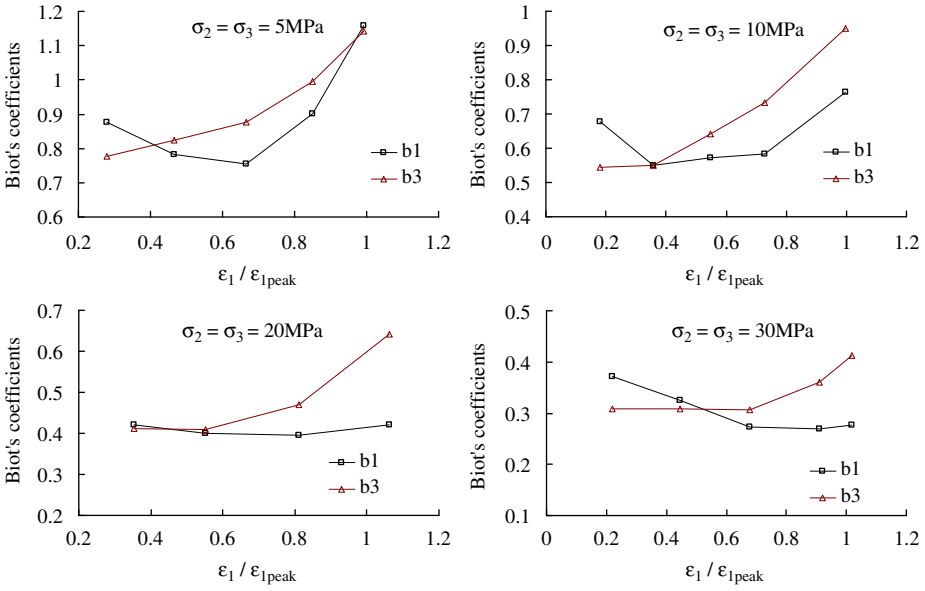

Fig. 11. Evolutions of Biot's coefficients in axial and radial directions with relative axial strain for different confining pressures.

depends on the range of permeability to be determined. Generally, for materials with relatively higher permeability (say $> 10^{-16}$ m^2), it is easy to reach the permanent flow regime and the steady-state flow is preferred. On the opposite side, for rocks with low and very low permeability, the set up of the steady-state flow needs a very long time period and it is then technically impossible to directly estimate the permeability. An indirect method, the most largely used one is called the pulse test method [3,39], is needed. The permeability is estimated from the pressure evolution with time, using an inverse numerical algorithm.

In the case of the sandstone studied here, its initial permeability is relatively high and estimated as about 10^{-16} m^2. We have then adopted the steady-state flow method. The principle of the test is very simple. It consists in the injection of water from the inlet surface of the sample in order to obtain an incremental variation of the interstitial pressure (Δp) while the pressure at the outlet surface is kept constant. When the steady-state flow is established, the pressure gradient (Δp) and the injection fluid rate, noted as Q (m^3 s^{-1}), become constant in time. Applying the classic Darcy's law, the intrinsic permeability (noted as k) can be easily deduced by

$$k(m^2) = \frac{Q\mu L}{\Delta p A} \tag{10}$$

The coefficient μ denotes the dynamic fluid viscosity coefficient and equals to $\mu = 1.005 \times 10^{-3}$ Pa s under the room temperature, L and A are the length and cross section of the sample, respectively.

Note that the objective here is to determine the rock permeability at different states of induced damage. Therefore, unloading–reloading cycles are performed for different levels of deviatoric stress. And the permeability is measured at the

beginning of unloading and reloading. The average flow rate used is about 0.07 ml/min.

7.2. Results and analysis

The typical stress–strain curves obtained in the triaxial tests for permeability measurement are plotted in Fig. 12. These curves complete those obtained in the monotonous tests and cyclic tests for Biot's coefficient determination presented in the previous sections. In an overall way, these results confirm the general trends previously obtained concerning the mechanical behaviour of the sandstone.

In Fig. 12, we also plotted the variations of the intrinsic permeability with the relative axial strain ($\varepsilon_1/\varepsilon_1^{peak}$). Note that only the permeability in the axial direction is measured due to the technical limitation of the device. However, as the induced microcracks are mainly oriented in the axial direction, the permeability in this direction should be more significantly affected than that in the radial direction. According to the obtained results, the most important feature of the permeability variation seems to be that the permeability decreases quite quickly during the two first stages of rock deformation, say the closure phase of initial bedding planes and microcracks and the linear elastic deformation phase. After then, with the onset and propagation of induced microcracks, the diminution of permeability is attenuated and an increase of permeability is even observed under low confining pressures. Such results seem to indicate that due to the relatively high value of the initial permeability of the sandstone, the variation of the permeability is more sensitive to the closure of bedding planes and initial microcracks than to the growth of induced damage. The effect of induced damage on the sandstone permeability becomes significant only at the late stage of induced damage approaching to the coalescence of microcracks. Further, it is also interesting to

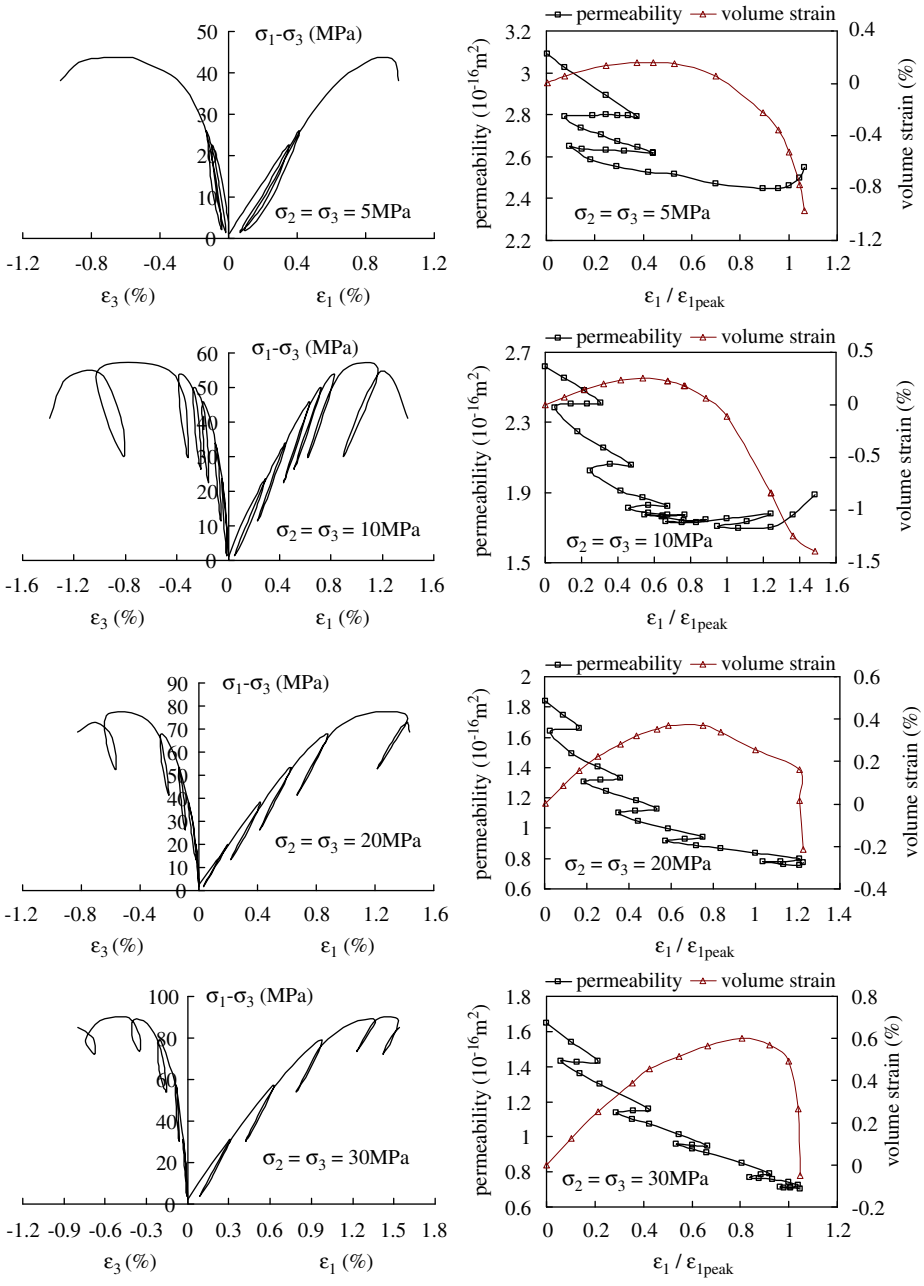

Fig. 12. Stress–strain curves, variations of permeability and volumetric deformation during triaxial tests for permeability measurement.

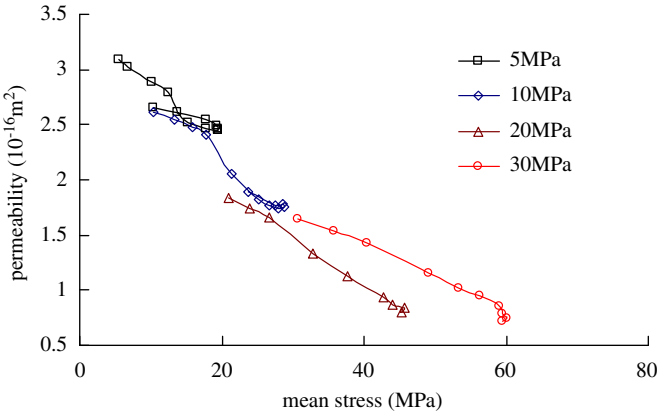

Fig. 13. Relationship between intrinsic permeability and effective mean stress during triaxial compression tests with different confining pressure.

look at the permeability variation during the unloading–reloading cycle. The permeability increases slightly during the unloading stage and then decreases more significantly during the reloading stage. The permeability at the end of unloading does not recover its initial value before loading. These results highlight the hysteretic behaviours of crack opening-closure leading to time-dependent responses. In the present work and as a first approach, the testing procedure is based on the assumption of time-independent poroelastic theory. The present work should be completed by other measurements such as ultrasonic technique or by averaging a large number of small loading/unloading cycles (oscillations), in order to eliminate the visco-elastic behaviour of crack opening and closing.

In addition, we have also studied the correlation between the permeability change and the cumulated volumetric strain as well as the applied mean stress σ_m at each point of unloading. The obtained results are plotted in Figs. 12 and 13. We can see that the axial permeability first decreases with the volumetric compressive strain. After the transition point of compaction-dilatancy, the axial permeability decreases with smaller rate and finally begins to increase. Therefore, there exists some correlation between permeability change and volumetric deformation. However, the permeability increase with the volumetric dilatancy is not as significant as a priori expected. On the other hand, it seems that the permeability continuously decreases with applied effective mean stress. Further, the observation on the permeability evolution in this work is in good agreement with those of [25,35], which found that the permeability of porous sandstones is reduced by shear stress enhanced pore compaction. Also, the permeability diminution is correlated with the increase of wave velocity during the closure of initial microcracks and pore compaction. The wave velocity remains nearly constant during the linear elastic phase and finally decreases with the significant growth and coalescence of microcracks.

8. Conclusions

In this paper, we have investigated the mechanical behaviour, Biot's coefficient and intrinsic permeability of sandstone in saturated conditions and with induced anisotropic damage. Hydrostatic compression tests and three series of triaxial tests with different confining pressures have been performed. The studied sandstone exhibits a slight structural anisotropy due to the existence of parallel bedding planes and initial microcracks. Under compressive stresses, these initial defeats are progressively closed leading to nonlinear stress–strain relations. Under applied deviatoric stress and after certain threshold, there is propagation of existing microcracks and nucleation of new ones. The propagation of microcracks is mainly oriented in the axial direction in conventional triaxial compression tests. The main consequences of the induced damage include the deterioration of elastic properties and induced anisotropy, strong sensitivity to confining pressure, transition from volumetric compressibility to dilatancy, anisotropic variation of Biot's coefficient and also intrinsic permeability. There is also the transition from brittle to ductile behaviour due to the diminution of induced damage rate under higher confining pressure. The oriented induced damage affects Biot's coefficient much more significantly in the axial direction than in the lateral one. There exists also some correlation between the permeability change and volumetric deformation as well as effective mean stress. However, the influence of volumetric dilatancy on the permeability increase is not very significant during the diffuse regime of damage. It seems that the induced damage will affect the rock permeability in a significant way only after the coalescence of microcracks. This important feature needs further investigations. Based on the present experimental work, it is proposed to formulate a coupled poroelastic damage model in order to take into account the coupling between rock deformation and the evolutions of poroelastic properties and permeability.

Acknowledgement

This study is partially supported by a NSFC international cooperation project through the Grant no. 50920105908.

References

[1] Biot MA. General theory of three dimensional consolidation. J Appl Phys 1941;12:155–64.
[2] Biot MA. Theory of elasticity and consolidation for a porous anisotropic solid. J Appl Phys 1955;26:182–5.
[3] Brace WF, Walsh JB, Frangos WT. Permeability of granite under high pressure. J Geophys Res 1968;73:2225–36.
[4] Dropek RK, Johnson JN, Walsh JB. The influence of pore pressure on the mechanical properties of Kayenta sandstone. J Geophys Res 1978;83: 2817–24.
[5] Green DH, Wang HF. Fluid pressure response to undrained compression in saturated sedimentary rock. Geophysics 1986;51:948–56.
[6] Fabre D, Gustkiewicz J. Poroelastic properties of limestones and sandstones under hydrostatic conditions. Int J Rock Mech Min Sci 1997;34(1):127–34.
[7] Hart DJ, Wang HF. A single test method for determination of poroelastic constants and flow parameters in rocks with low hydraulic conductivities. Int J Rock Mech Min Sci 2001;38:577–83.
[8] Lion M, Skoczylas F, Ledesert B. Determination of the main hydraulic and poro-elastic properties of a limestone from Bourgogne, France. Int J Rock Mech Min Sci 2004;41:915–25.
[9] Trautwein U, Huenges E. Poroelastic behaviour of physical properties in Rotliegend sandstones under uniaxial strain. Int J Rock Mech Min Sci 2005; 42:924–32.
[10] Ghabezloo S, Sulem J, Guedon S, Martineau F. Effective stress law for the permeability of a limestone. Int J Rock Mech Min Sci 2009;46:297–306.
[11] Carroll MM. An effective stress law for anisotropic elastic deformation. J Geophys Res 1979;84:7510–2.
[12] Brace WF, Martin RJ. A test of the law of effective stress for crystalline rocks of low porosity. Int J Rock Mech Min Sci 1968;5:415–26.
[13] Tapponier P, Brace WF. Development of stress-induced microcracks in Westerly granite. Int J Rock Mech Min Sci 1975;12:103–12.
[14] Wong TF. Micromechanics of faulting in Westerly granite. Int J Rock Mech Min Sci 1992;19:49–64.
[15] Moore DE, Lockner DA. The role of microcracking in shear fracture propagation in granite. J Struct Geol 1995;17:95–114.
[16] Wong TF, David C, Zhu W. The transition from brittle faulting to cataclastic flow in porous sandstones: mechanical deformation. J Geophys Res 1997;102(B2):3009–25.
[17] Baud P, Schubnel A, Wong TF. Dilatancy, compaction, and failure mode in Solnhofen limestone. J Geophys Res 1999;105(B8):19289–303.
[18] Ismail IAH, Murell SAF. Dilatancy and the strength of rocks containing pore water under undrained conditions. Geophys J R Astr Soc 1976;S44:107–34.
[19] Steif PS. Crack extension under compressive loading. Eng Fract Mech 1984; 20(3):463–73.

[20] Horii H, Nemat-Nasser S. Compression-induced microcrack growth in brittle solids: axial splitting and shear failure. J Geophys Res 1985;90(B4):3105–25.
[21] Fredrich JT, Evans B, Wong TF. Micromechanics of the brittle to plastic transition in Carrara marble. J Geophys Res 1989;94:4129–45.
[22] Schmitt DR, Zoback MD. Diminished pore pressure in low-porosity crystalline rock under tensional failure: apparent strengthening by dilatancy. J Geophys Res 1992;97:273–88.
[23] Olsson W. Development of anisotropy in the incremental shear moduli for rock undergoing inelastic deformation. Mech Mater 1995;21:231–42.
[24] Shao JF, Rudnicki JW. A microcrack-based continuous damage model for brittle geomaterials. Mech Mater 2000;32:607–19.
[25] Zhu W, Montesi L, Wong TF. Shear-enhanced compaction and permeability reduction: triaxial extension tests on porous sandstone. Mech Mater 1997; 25:199–214.
[26] Suzuki K, Oda M, Yamazaki M, Kuwahara T. Permeability changes in granite with crack growth during immersion in hot water. Int J Rock Mech Min Sci 1998;35(7):907–21.
[27] Schulze O, Popp T, Kern H. Development of damage and permeability in deforming rock salt. Eng Geol 2001;61:163–80.
[28] Souley M, Homand F, Pepa S, Hoxha D. Damage-induced permeability changes in granite: a case example at the URL in Canada. Int J Rock Mech Min Sci 2001;38:297–310.
[29] Bossart P, Meier PM, Moeri A, Trick T, Mayor JC. Geological and hydraulic characterisation of the excavation disturbed zone in the Opalinus Clay of the Mont Terri Rock Laboratory. Eng Geol 2002;66:19–38.
[30] Wang JA, Park HD. Fluid permeability of sedimentary rocks in a complete stress–strain process. Eng Geol 2002;63:291–300.
[31] Oda M, Takemura T, Aoki T. Damage growth and permeability change in triaxial compression tests of Inada granite. Mech Mater 2002;34:313–31.
[32] Shao JF, Zhou H, Chau KT. Coupling between anisotropic damage and permeability variation in brittle rocks. Int J Numer Anal Meth Geomech 2005;29:1231–47.
[33] Guéguen Y, Schubnel A. Elastic wave velocities and permeability in cracked rocks. Tectonophysics 2003;370:163–76.
[34] Fortin J, Guéguen Y, Schubnel A. Consequences of pore collapse and grain crushing on ultrasonic velocities and *Vp*/*Vs* ratio. J Geophys Res 2007; 112(B8):B08207.
[35] Fortin J, Schubnel A, Guéguen Y. Elastic wave velocities and permeability evolution during compaction of Bleuswiller sandstone. Int J Rock Mech Min Sci 2005;42:873–89.
[36] Schubnel A, Guéguen Y. Anisotropy and dispersion of elastic waves in cracked rocks. J Geophys Res 2003;108(B2):2101.
[37] Secq J. Collier de mesure de la déformation latérale d'une éprouvette lors d'essais de compression, notamment uniaxiale ou triaxiale- collier à lame. French Patent No. 0505204, 2006.
[38] Fortin J, Stanchits S, Dresen G, Gueguen Y. Acoustic emissions monitoring during inelastic deformation of porous sandstone: comparison of three modes of deformation. Pure Appl Geophys 2009;166(5-7):823–41.
[39] Coussy O. Mechanics of Porous Continua. New York: Wiley; 1995.
[40] Zimmerman RW. Coupling in poroelasticity and thermoelasticity. Int J Rock Mech Min Sci 2000;37:79–87.
[41] Thompson M, Willis JR. A reformulation of the equations of anisotropic poroelasticity. J Appl Mech 1991;58:612–6.
[42] AHD Cheng. Material coefficients of anisotropic poroelasticity. Int J Rock Mech Min Sci 1997;34(2):199–205.
[43] Shao JF. Poroelastic behaviour of brittle rock materials with anisotropic damage. Mech Mater 1998;30:41–53.
[44] Lydzba D, Shao JF. Study of poro-elasticity material coefficients as response of microstructure. Mech Cohesive-Frictional Mater 2000;5:149–71.
[45] Sayers CM, Kachanov M. Microcrack-induced elastic wave anisotropy of brittle rocks. J Geophys Res 1995;100(B3):4149–56.
[46] Zhu W, Montesi LGJ, Wong TF. Shear-enhanced compaction and permeability reduction: triaxial extension tests on porous sandstone. Mech Mater 1997; 25:199–214.